Supporting Information

Development of polyoxometalate-based Ag-H_2biim inorganic-organic hybrid compounds functionalized for acid electrocatalytic hydrogen evolution reaction

Sifan Li, [a,c] Jiansheng Li,[a,b,*] Haotian Zhu,[a] Liyuan Zhang,[a] Xiaojing Sang,[a] Zaiming Zhu,[a] Wansheng You[a*] and Fuxiang Zhang[b*]

[a] School of Chemistry and Chemical Engineering, Liaoning Normal University, Dalian 116029, Liaoning, China

[b] State Key Laboratory of Catalysis, iChEM, Dalian Institute of Chemical Physics, Chinese Academy of Sciences, Dalian National Laboratory for Clean Energy Dalian 116023, Liaoning, China

[c] Department of Biochemical Engineering, Chaoyang Techers College, Chaoyang 122000, Liaoning, China

Contents

1 Synthesis of compounds 1 and 2

1.1 Synthesis of $\{[(Ag_2(H_2biim)(H_2biimCOO))_2H_2(SiW_{12}O_{40})]\cdot 4H_2O\}_n$ (1)

$AgNO_3$ (0.100 g, 0.59 mmol) and H_2biim (0.028 g, 0.20 mmol) were dissolved in 8 mL distilled water and stirred for 10 minutes at room temperature to form solution A. $H_4[\alpha\text{-}SiW_{12}O_{40}]\cdot 12H_2O$ (0.190 g, 0.06 mmol) was dissolved in 7 mL distilled water to form solution B, which was added to solution A drop by drop. After stirring continuously for 2.5 h, the mixture was transferred into 20 mL Teflon-lined autoclave and heated at 160 °C for 4 days. The autoclave was cooled to 25 °C with the rate of 10 °C h^{-1}. Yellow block crystals of compound **1** were filtered, then washed with water and dried at room temperature (Yield: 56% based on W). Elemental analysis calculated for $C_{26}H_{34}Ag_4N_{16}O_{48}SiW_{12}$ (4003.65): Si, 0.70%; W, 55.10%; Ag, 10.78%. Elements ratio found: Si, 0.75%; W, 55.20%; Ag, 10.80%. IR (KBr pellet, cm^{-1}): 3565 (br), 3139 (m), 1714 (w), 1622 (m), 1544 (w), 1514 (m), 1377 (m), 1244 (m), 1114 (m), 1018 (m), 972 (s), 923 (s), 802 (s).

1.2 Synthesis of $\{K_2[(Ag_2(H_2biim)_2)_2(P_2W_{18}O_{62})]\cdot 2H_2O\}_n$ (2).

The synthesis method of compound **2** is similar to that of compound **1**, except that $AgNO_3$ (0.260 g, 0.15 mmol) and H_2biim (0.067 g, 0.50 mmol) were dissolved in solution A and $K_6[\alpha\text{-}P_2W_{18}O_{62}]\cdot 14H_2O$ (0.400 g, 0.08 mmol) was dissolved in solution B. Red hexagonal crystal of compound **2** were filtered, then washed with water and dried at room temperature (Yield: 49% based on W). Elemental analysis calculated for $C_{24}H_{28}Ag_4K_2N_{16}O_{64}P_2W_{18}$ (5441.51): K, 1.43%; P, 1.14%; W, 60.78%; Ag, 7.92 %. Elements ratio found: K, 1.42%; P, 1.15%; W, 60.80%; Ag, 7.90%. IR (KBr pellet, cm^{-1}): 3455 (br), 3244 (m), 3138 (w), 1620 (m), 1536 (m), 1418 (m), 1336 (w), 1292 (w), 1222 (w), 1088 (s), 950 (s), 901 (s), 801 (s).

1.3 Single Crystal X-ray Crystallography.

Single-crystal X-ray data of compounds **1** and **2** were collected at room temperature and corrected by LP factor and empirical absorption. The coordinates of all non-hydrogen atoms were solved by direct methods and refined by full-matrix least-squares. The hydrogen atoms were placed on the calculated positions. All calculations were completed by SHELXTL-2014 program.[1]

2. Crystal data and refinement parameters

Table S1. Crystal data and structure refinements for compounds **1** and **2**

Compound	**1**	**2**
Formula	$C_{26}H_{32}Ag_4N_{16}O_{48}SiW_{12}$	$C_{24}H_{28}Ag_4K_2N_{16}O_{64}P_2W_{18}$
Formula weight	4002.44	5441.51
T/K	296(2)	296(2)
Crystal system	Monoclinic	Orthorhombic
Space group	$P2_{1/n}$	*Cmcm*
a/Å	14.113(7)	21.5725(10)
b/Å	15.931(8)	11.9328(5)
c/Å	15.581(8)	32.2060(15)
α/°	90.00	90.00
β/°	94.238(7)	90.00
γ/°	90.00	90.00
V/nm^3	3.494(3)	8.2905(6)
Z	2	4
μ/mm^{-1}	20.881	26.027
F (000)	3548	9536
Total reflections	18177	19109
R_{int}	0.0450	0.0544
GOF	1.068	1.098
$R_1[I>2\sigma(I)]$[a]	0.0434	0.0638
wR_2 (all data)[b]	0.1051	0.1922

[a]$R_1=\sum||F_o|-|F_c||/\sum|F_o|$, [b]$wR_2=\sum[w(F_o^2-F_c^2)^2]/\sum[w(F_o^2)^2]^{1/2}$

3. Crystal structure

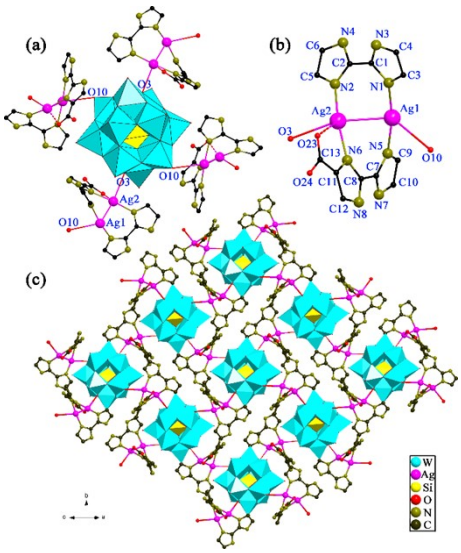

Fig. S1 (a) The tetra-supported polyoxoanion structure in **1** and (b) the $[Ag_2(H_2biim)_2COO]^+$ complex unit in **1** and (c) the infinite 2-D layer framework of **1**.

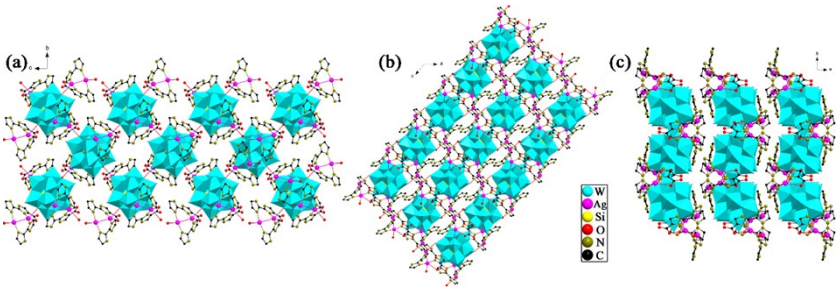

Fig. S2 Polyhedral and ball-and-stick representation of 3D structure of compound **1** packing arrangement along a (a), b (b), and c (c) axes, respectively.

In compound **1**, each Keggin-type polyoxoanion acts as a tetradentate ligand that coordinates with four Ag(I) ions via two terminal oxygen atoms (O10, O10') and two bridging oxygen atoms (O3, O3') to form a tetra-supported structure (Fig. S1a). This multi-supported structure may play a key role in stabilizing the compound. In **1**, there are two crystallographic independent Ag(I) centers, i.e. Ag1 and Ag2 (Fig. S1b). It is shown that in $[Ag_2(H_2biim)_2COO]^+$, each Ag1 center adopts four-coordination mode, which coordinates with Ag2 and two nitrogen atoms (N1, N5) from two different H_2biim ligands and one oxygen atom (O10) from SiW_{12}. For Ag1, the bond lengths of Ag1–Ag2, Ag1–N1, Ag1–N5 and Ag1–O10 are 2.852(3) Å, 2.118(14) Å, 2.143(14) Å and 2.636(2) Å, respectively (Table S2). Ag2 adopts five-coordination mode, which coordinates with Ag1, two nitrogen atoms (N2, N6) from two different H_2biim ligands, one oxygen atom (O3) from SiW_{12} and one oxygen atom (O23) from the COO group. The bond lengths of Ag2–N2, Ag2–N6, Ag2–O3 and Ag2–O23 are 2.115(14) Å, 2.16(2) Å, 2.623(2) Å and 2.7863(3) Å, respectively (Table S2). It is noted that a closed five-membered ring forms through connection of Ag2, N6, C11, C13 and O23 atoms.

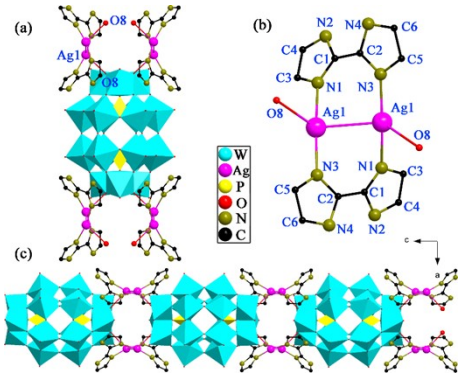

Fig. S3 (a) The tetra-supported polyoxoanion structure in **2** and (b) the $[Ag_2(H_2biim)_2]^{2+}$ complex unit in **2** and (c) the infinite 1-D chain of **2**.

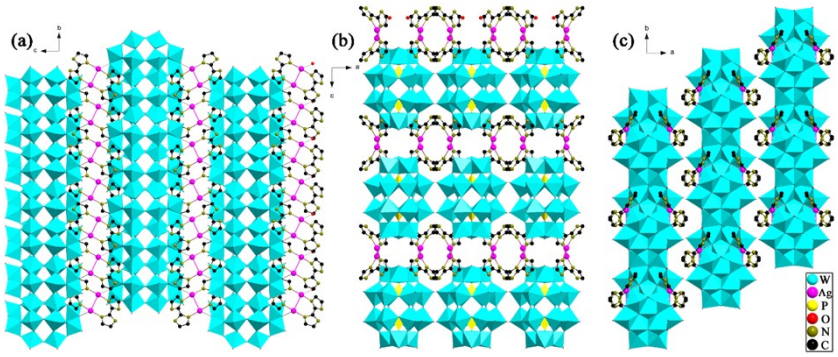

Fig. S4 Polyhedral and ball-and-stick representation of 3D structure of compound **2** packing arrangement along a (a), b (b), and c (c) axes, respectively.

In **2**, P_2W_{18} acts as a tetradentate ligand which coordinates with four Ag(I) ions via two bridging oxygen atoms (O8, O8′) to form a tetra-supported structure (Fig. S3a). There is one crystallographic independent Ag1 center (Fig. S3b). In $[Ag_2(H_2biim)_2]^{2+}$, each Ag1 coordinates with the other Ag1, two nitrogen atoms (N1, N3) from different H_2biim ligands and one oxygen atom (O8) from P_2W_{18} unit, with the bond length of Ag1–Ag1, Ag1–N1, Ag1–N3 and Ag1–O8 of 2.858(3) Å, 2.130(2) Å, 2.11(3) Å and 2.837(2) Å, respectively. The W–O distances are in the range of 1.684(12) Å–2.432(14) Å (Table S4).

4. Selected bond lengths and angles

Table S2 Selected bond lengths (Å) and bond angles (°) of compound **1**

Bond	Length(Å)	Bond	Length(Å)	Bond	Length(Å)
Ag1−N5	2.143(14)	Si1−O6	1.667(9)	N5−C9	1.36(2)
Ag1−N1	2.118(14)	Si1−O6#1	1.667(9)	N6−C11	1.369(18)
Ag1−Ag2	2.852(3)	O2A−O2	0.83(2)	N6−C8	1.30(2)
Ag2−N2	2.115 (14)	O2− O13#1	1.81(3)	N7−C7	1.34(2)
Ag2−N6	2.16(2)	O23−C13	1.231(19)	N7−C10	1.347(19)
Ag2−O23	2.7863(3)	O24−C13	1.217(17)	N8−C12	1.33(2)
Ag2−O3	2.623(2)	N1−C1	1.35(2)	N8−C8	1.40(2)
Ag1−O10	2.636(2)	N1−C3	1.35(2)	C1−C2	1.42(2)
Si1−O5#1	1.506(19)	N2−C2	1.351(19)	C3−C4	1.33(2)
Si1−O5	1.507(19)	N2−C5	1.40(2)	C5−C6	1.32(2)
Si1−O20#1	1.55(3)	N3−C1	1.36(2)	C7−C8	1.42(2)
Si1−O4#1	1.512(18)	N3−C4	1.36(2)	C9−C10	1.33(2)
Si1−O4	1.512(18)	N4−C2	1.35(2)	C11−C13	1.36(2)
Si1−O7	1.650(19)	N4−C6	1.34(2)	C11−C12	1.35(2)
Si1−O7#1	1.650(19)	N5−C7	1.326(19)		
Bond	**Angle(°)**	**Bond**	**Angle(°)**	**Bond**	**Angle(°)**
O5#1−Si1−O5	180.0	C3−N1−Ag1	125.8(13)	C3−C4−N3	107.1(17)
O4#1−Si1−O4	180.0	C2−N2−C5	105.4(13)	C6−C5−N2	109.1(15)
O4#1−Si1−O7	114.0(10)	C2−N2−Ag2	125.0(11)	O3−Ag2−Ag1	149.5(10)
O4−Si1−O7	66.0(10)	C5−N2−Ag2	129.6(10)	O23−Ag2−O3	74.9(9)
O4#1−Si1−O7#1	66.0(10)	C1−N3−C4	108.0(16)	C13−O23−Ag2	108.3(10)
O4−Si1−O7#1	114.0(10)	C6−N4−C2	109.2(14)	C5-C6-N4	107.8(16)
O7−Si1−O7#1	180.0(13)	C7−N5−C9	106.4(14)	N5−C7−N7	109.9(14)
O5#1−Si1−O6	74.3(9)	C7−N5−Ag1	128.4(11)	N5−C7−C8	126.4(16)
O5−Si1−O6	105.7(9)	C9−N5−Ag1	125.1(11)	N7−C7−C8	123.7(15)
O5#1−Si1−O6#1	105.7(9)	C8−N6−C11	105.2(14)	N6−C8−N8	110.8(14)
O5−Si1−O6#1	74.3(9)	C8−N6−Ag2	129.5(10)	N6−C8−C7	127.7(15)
O6−Si1−O6#1	180.0	C11−N6−Ag2	124.6(11)	N8−C8−C7	121.5(16)
N1−Ag1−N5	168.1(5)	C7−N7−C10	107.0(14)	C10−C9−N5	108.6(15)
N1−Ag1−Ag2	81.7(4)	C12−N8−C8	106.5(15)	C9−C10−N7	108.1(16)
N5−Ag1−Ag2	86.4(4)	N1−C1−N3	107.7(14)	C12−C11−C13	127.1(15)
N2−Ag2−N6	167.9(5)	N1−C1−C2	126.9(16)	C12−C11−N6	110.6(15)
N2−Ag2−Ag1	86.0(4)	N3−C1−C2	125.3(17)	C13−C11−N6	122.1(16)
N6−Ag2−Ag1	84.2(3)	N4−C2−N2	108.5(15)	N8−C12−C11	106.9(15)
Si1−O4−O7	60.8(9)	N4−C2−C1	126.1(15)	O24−C13−O23	120.7(17)
C1−N1−C3	107.1(15)	N2−C2−C1	125.4(15)	O24−C13−C11	120.3(17)
C1−N1−Ag1	127.1(11)	C4−C3−N1	110.1(18)	O23−C13−C11	118.8(15)

Symmetry transformations used to generate equivalent atoms: #1 −x+1, −y+1, −z+1

Table S3 Hydrogen bonds for compound **1**

D–H···A	d(D–H) (Å)	d(H···A) (Å)	d(D···A) (Å)	∠(DHA) (°)
N(3)−H(3A)...O(4W) #2	0.86	1.83	2.68(5)	170.7
N(4)−H(4A)...O(14A)#3	0.86	2.28	3.09(2)	156.2
N(7)−H(7A)...O(5W) #4	0.86	1.93	2.74(2)	156.5
N(8)−H(8A)...O(2W)	0.86	1.83	2.68(5)	170.7

Symmetry transformations used to generate equivalent atoms: #2 −x+1, −y+2, −z+1 #3 x−1/2, −y+3/2, z+1/2 #4 −x+3/2, y−1/2, −z+3/2

Table S4 Selected bond lengths (Å) and bond angles (°) of compound **2**

Bond	Length(Å)	Bond	Length(Å)	Bond	Length(Å)
Ag1−N3	2.113(16)	W3−O6	1.909(11)	P1−O9	1.528(10)
Ag1−N1#1	2.144(17)	W3−O7	1.916(8)	P1−O9#2	1.528(10)
W1−O1	1.718(11)	W3−O8	1.930(11)	P1−O14	1.534(16)
W1−O3	1.900(12)	W3−O14	2.400(10)	P1−O10	1.547(16)
W1−O16	1.903(10)	W4−O17	1.719(11)	N1−C1	1.28(2)
W1−O2	1.905(2)	W4−O16	1.898(10)	N1−C3	1.37(3)
W1−O6	1.913(12)	W4−O20	1.900(2)	N2−C1	1.33(2)
W1−O9	2.357(9)	W4−O19	1.911(7)	N2−C4	1.37(3)
W2−O5	1.689(17)	W4−O18	1.919(11)	N3−C2	1.33(2)
W2−O4#2	1.919(11)	W4−O10	2.346(11)	N3−C5	1.36(3)
W2−O4	1.919(11)	W5−O13	1.726(12)	N4−C6	1.33(3)
W2−O8	1.922(11)	W5−O11	1.896(4)	N4−C2	1.40(3)
W2−O8#2	1.922(11)	W5−O12	1.900(2)	C1−C2	1.45(3)
W2−O14	2.432(14)	W5−O4	1.901(12)	C3−C4	1.30(3)
W3−O15	1.684(12)	W5−O3	1.901(11)	C5−C6	1.33(3)
W3−O18	1.907(12)	W5−O9	2.378(10)		
Bond	**Angle(°)**	**Bond**	**Angle(°)**	**Bond**	**Angle(°)**
N3−Ag1−N14	168.4(7)	O18−W3−O6	85.1(5)	C1−N2−C4	106.3(16)
O1−W1−O9	173.6(5)	O17−W4−O10	173.5(5)	C2−N3−C5	107.4(16)
O2−W1−O6	163.9(5)	O20−W4−O18	163.2(5)	C2−N3−Ag1	126.5(13)
O16−W1−O2	87.0(5)	O19−W4−O10	73.3(5)	C6−N4−C2	106.9(19)
O3−W1−O9	73.1(4)	O16−W4−O20	86.6(5)	N1−C1−N2	109.4(16)
O5−W2−O14	172.2(7)	O13−W5−O9	173.1(5)	N2−C1−C2	122.2(17)
O4#2−W2−O8	155.9(5)	O12−W5−O4	163.6(5)	N3−C2−N4	107.9(17)
O82−W2−O14	73.2(4)	O3−W5−O9	72.6(4)	N4−C2−C1	124.5(17)
O4#2−W2−O4	84.7(7)	O11−W5−O12	87.1(6)	C4−C3−N1	107(2)
O15−W3−O14	172.3(5)	O9−P1−O9#2	112.5(8)	C3−C4−N2	108.0(19)
O18−W3−O8	155.9(5)	O14−P1−O10	106.3(8)	C6−C5−N3	109(2)
O7−W3−O14	73.2(5)	C1−N1−C3	108.7(18)	N4−C6−C5	109(2)

Symmetry transformations used to generate equivalent atoms: #1+x, 1−y, −z; #2 1−x, +y, +z

Table S5 Hydrogen bonds for compound **2**

D–H...A	d(D–H) (Å)	d(H...A) (Å)	d(D...A) (Å)	<(DHA) (°)
N2−H2A...O1#1	0.86	2.03	2.85(2)	159.4
N4−H4A...O13	0.86	2.13	2.86(2)	142.3
N4−H4A...O17#2	0.86	2.44	3.12(2)	135.4

Symmetry transformations used to generate equivalent atoms: #1 1/2−x, 1/2+y, +z; #2 +x, 1+y, +z

5. Characterization of compounds 1 and 2

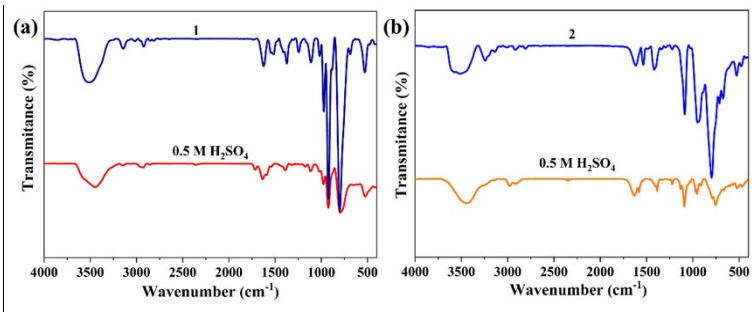

Fig. S5 FTIR spectra of compounds (a) **1** and (b) **2** before and after immersing in 0.5 M H_2SO_4 for 10 h.

The characteristic bands in the range of 713−1088 cm^{-1} are attributed to ν(W–O_b–W)/ν(W–O_c–W)/ ν(W–O_d)/ν(Si–O_c)/ν(P–O_a) of the polyoxoanions (O_b = bridged oxygen of two octahedra sharing a corner, O_c = bridged oxygen of two octahedra and O_d = terminal oxygen).[2,3] The bands in the range of 1114−3244 cm^{-1} are attributed to ν(C−N)/ν(C=C)/ν(C=N)/ν(N−H)/ν(C−H) of H_2biim, and the specific attributions are shown in Table S6.

Table S6 FTIR peak assignments of compounds **1** and **2**

Compound **1**		Compound **2**	
802	W–O_c–W	801	W–O_c–W
923	W–O_b–W	901	W–O_b–W
972	Si–O_c	950	W–O_d
1018	W–O_d	1088	P–O_c
1114	C−N	1222	C−N
1244	C−N	1292	C−N
1377	C−N	1336	C−N
1514	C=C	1418	C=C
1544	C=C	1536	C=C
1622	C=N	1620	C=N
1714	C=O	3138	N−H
3139	N−H	3244	C−H
3565	O−H	3455	O−H

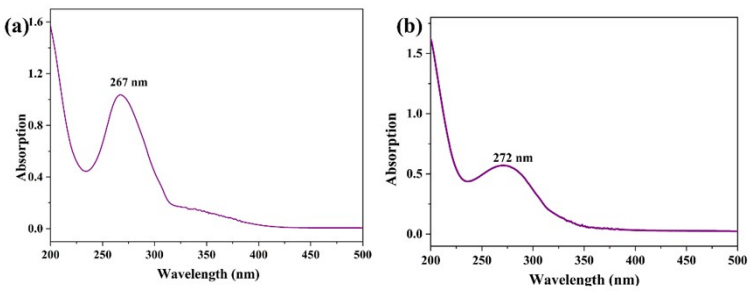

Fig. S6 UV-vis absorption spectra of compounds (a) **1** and (b) **2**.

The UV-vis absorption spectra of **1** and **2** (Fig. S6) shows good absorption peaks at 267 nm and 272 nm, respectively, which are ascribed to the $O_{b,c}$→W charge transfer.[4]

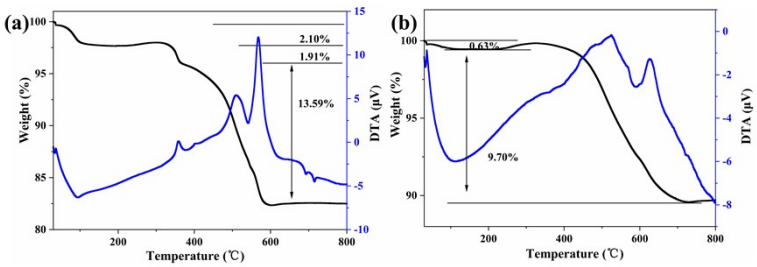

Fig. S7 TG curves for compounds (a) **1** and (b) **2**.

The thermal stability of **1** and **2** were investigated under a N_2 atmosphere from 0 to 800 °C, and the TG curves are provided in Fig. S7. For **1**, the weight loss of 2.10% (calcd 1.81%) in the range of 25−100 °C release of was attributed to the crystal water molecules. In the range of 100−360 °C, the weight loss of 1.91% (calcd 2.20%) was assigned to decomposition of organic component of the COO group. The weight loss of 13.59 % (calcd 13.39 %) at 360−590 °C corresponds to the decomposition of H_2biim. The whole weight loss (17.60 %) is in good agreement with the calculated value (17.39%). For **2**, the first weight loss of 0.63 % (calcd 0.67 %) below 100 °C were assigned to the removal of H_2O, and the second continuous weight losses of 9.70 % (calcd 9.92%) at 100−720 °C may be the decomposition of H_2biim ligands.

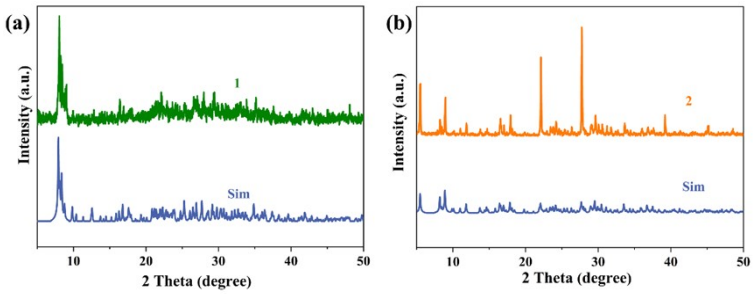

Fig. S8 PXRD spectra of compounds (a) **1** and (b) **2**.

The simulated and experimental PXRD of **1** and **2** are shown in Fig. S8. The experimental diffraction peaks are consistent with the simulated patterns, indicating the phase purity of **1** and **2**. The difference in intensity may be due to the destruction of lattice waters during grinding, which affects the surface morphology of the powder samples.

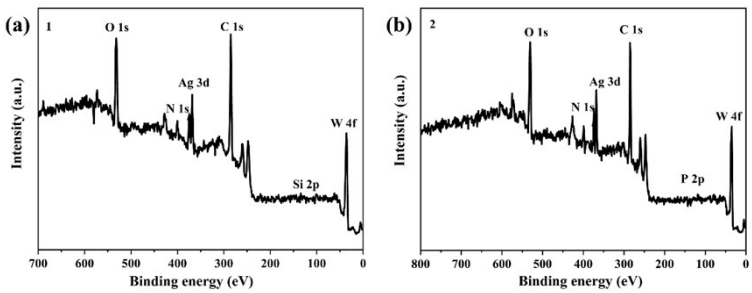

Fig. S9 XPS survey spectra of compounds (a) **1** and (b) **2**.

XPS was performed to probe the structural and chemical states of the elements present in **1** and **2**. The XPS survey spectrum indicates the presence of Ag, Si, W, O, N, C for **1** and Ag, P, W, O, N, C for **2** (Fig. S9).

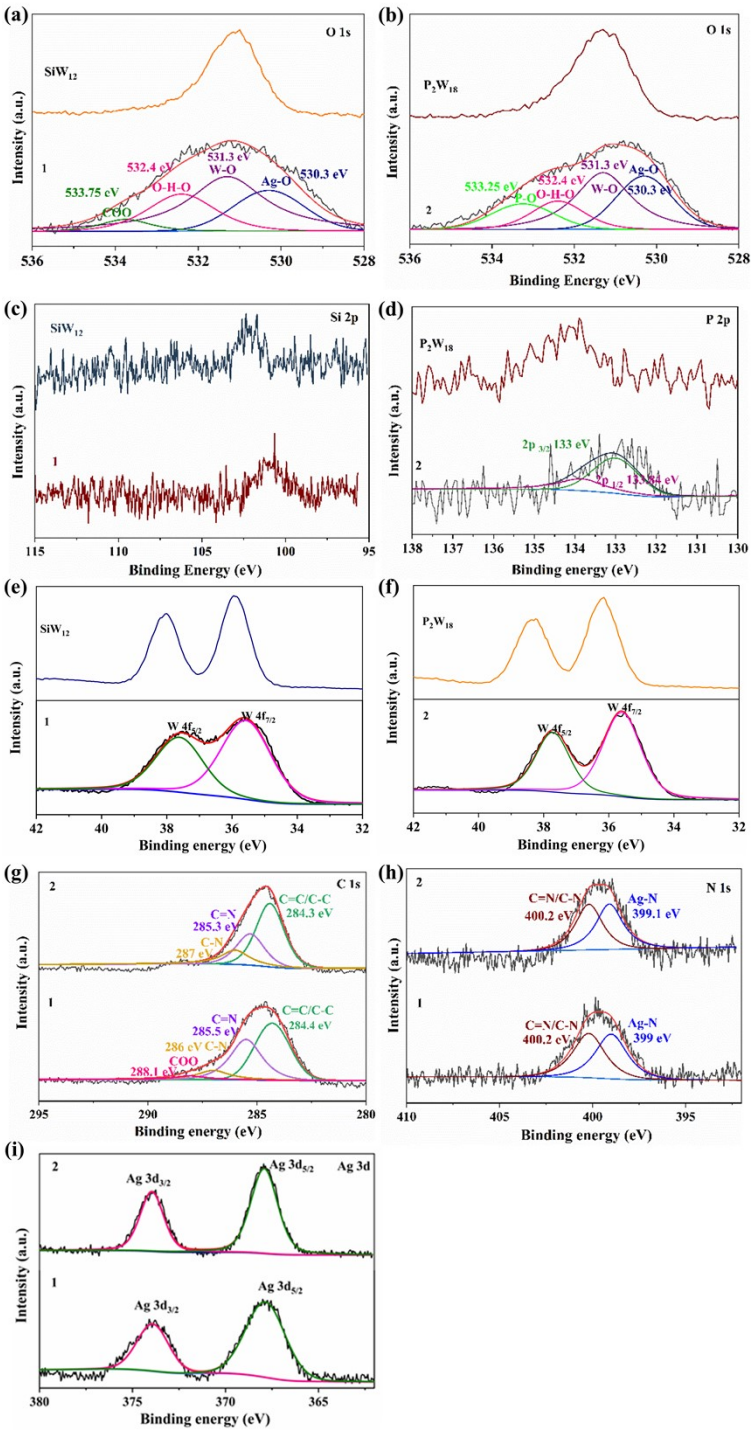

Fig. S10 XPS spectra for (a,b) O 1s, (c) Si 2p, (d) P 2p, (e,f) W 4f, (g) C 1s, (h) N 1s and and (i) Ag 3d of SiW_{12}, P_2W_{18}, compounds **1** and **2**, respectively.

As shown in Figure S10, compared with SiW_{12} and P_2W_{18}, it is noted that the peak positions for Si/W/O in **1** and P/W/O in **2** have all shifted to lower binding energy region, which is maybe due

to the interaction between POMs (SiW_{12} and P_2W_{18}) and Ag-H_2biim. In detail, the O 1s region indicates four distinct features assigned to Ag−O, W−O, COO and H−O−H bonds for **1**, Ag−O, W−O, P−O and H−O−H bonds for **2**, respectively (Fig. S10a and b).[5–7] The Si 2p for **1** and P 2p for **2** regions are presented in Fig. S10c and d. The W 4f region can be deconvoluted into two signals related to W $4f_{7/2}$ and W $4f_{5/2}$ peaks referring to the W (VI) oxidation state (Fig. S10e and f).[8] The C 1s region is fitted four peaks for **1**: C=C/C−C, C=N, C−N and COO bonds, three peaks for **2**: C=C/C−C, C=N, and C−N bonds (Fig. S10g), respectively. All the N 1s region is fitted into two peaks assigned to Ag−N and C=N/C−N bonds, respectively (Fig. S10h).[9,10] The typical peaks for Ag 3d at 367.9 and 373.9 eV are assigned to Ag $3d_{5/2}$ and Ag $3d_{3/2}$, respectively, which are indicative of Ag (I) in **1** and **2** (Fig. S10i).[11,12]

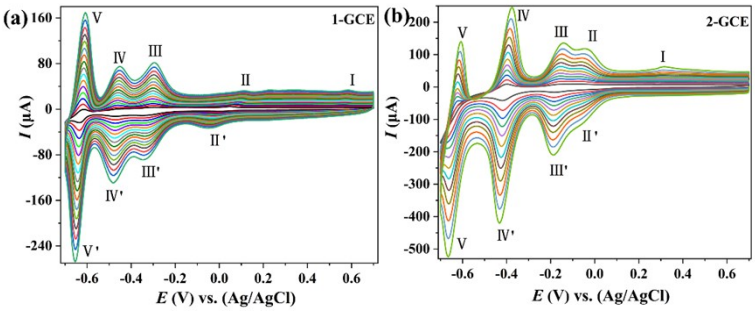

Fig. S11 CV curves of (a) **1**-GCE and (b) **2**-GCE in 0.1 M H_2SO_4 aqueous solution under scan rates from inner to outer: 25, 50, 75, 100, 125, 150, 175, 200, 225, 250, 275 and 300 mV s^{-1}.

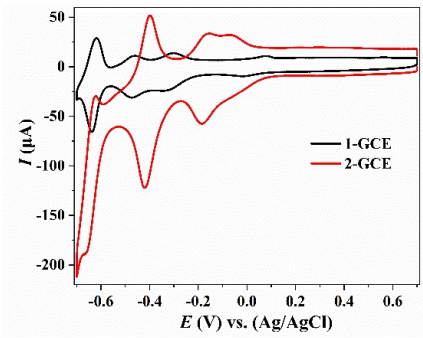

Fig. S12 CV curves of **1**-GCE and **2**-GCE in 0.1 M H_2SO_4 aqueous solution at 100 mV s^{-1}.

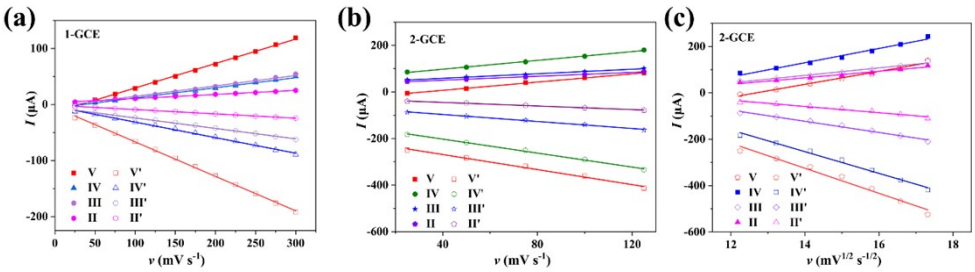

Fig. S13 The linear fit plots of the anodic and cathodic peak currents against scan rate for (a) **1**-GCE, (b) **2**-GCE and (c) against square root of scan rate for **2**-GCE, respectively.

The CV curves contain three (**1**-GCE) and four (**2**-GCE) pairs of reversible redox peaks, with the corresponding mean peak potentials ($E_{1/2}$ = (E_{pa} + E_{pc}) / 2) at −0.312 (III-III′), −0.466 (IV-IV′) and −0.63 (V-V′) V for **1,** −0.052 (II-II′), −0.173 (III-III′), −0.408 (IV-IV′) and −0.638 V (V-V′) for **2** (scan rate: 100 mV s^{-1}). The redox peaks can be ascribed to the redox process of W centers in the polyanions and the processes involved are in good agreement with the previously published works.[13,14]

The redox peak II-II′ (0.030 V) for **1** can be attributed to a Ag(I)/Ag(0) redox process. The other irreversible anodic peak I for **1** (0.562 V) and **2** (0.295 V) are assigned to the oxidation of the Ag(I).[15] In addition, the areas of the CV curve surrounding **1**-GCE and **2**-GCE at 100 mV s^{-1} are compared in Fig. S12. It can also be observed that the order of CV area is as **2**-GCE > **1**-GCE, indicating that **2** shows a larger capacitance than **1** at the same current density.[16] It is noted that **1**-GCE and **2**-GCE are stable, and the peak potentials change little with the increasing scan rates, which is especially useful for electrocatalytic studies. In plots of the redox peak currents of anode and cathode against scanning rates from 25 to 300 mV s^{-1}, for **1**-GCE, the peak currents are proportional to the scanning rates, indicating that the redox processes is surface-controlled (Fig. S13a).[17] For **2**-GCE, when the scan rates are lower than 150 mV s^{-1}, the peak currents are proportional to the scan rates, which indicates that the redox process is surface-controlled (Fig. S13b); however, when the scan rates are higher than 150 mV s^{-1}, the peak currents are proportional to the square root of the scan rate, which indicates that the redox process is diffusion-controlled (Fig. S13c).[15]

6. Electrocatalytic HER performance

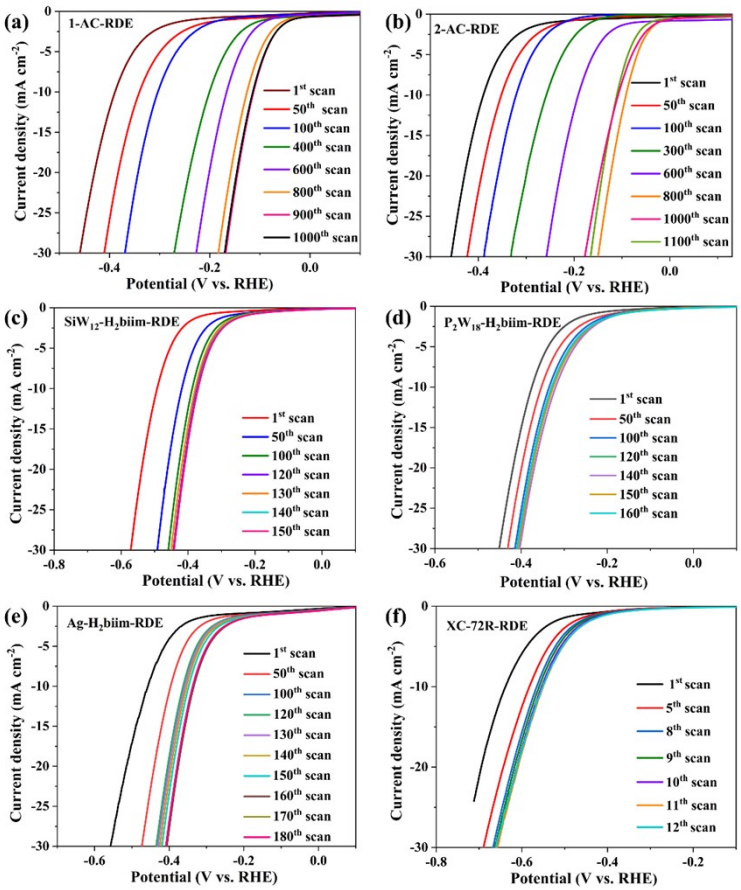

Fig. S14 LSV curves of (a) **1-**AC-RDE, (b) **2-**AC-RDE, (c) SiW_{12}-H_2biim-RDE, (d) P_2W_{18}-H_2biim-RDE, (e) Ag-H_2biim-RDE and (f) XC-72R-RDE after different times of successive CV cycles in 0.5 M H_2SO_4, scan rate: 5 mV s^{-1}.

Table S7 Comparison of HER performance of **1**-AC-RDE and **2**-AC-RDE with other POMs-based HER electrocatalysts in acidic electrolyte

Catalyst	Loading (mg cm^{-2})	Electrode	η_{10} (mV)	Tafel slope (mV dec^{-1})	Reference
1-AC-RDE	0.32	RDE	112	77	This work
2-AC-RDE	0.32	RDE	91	65	This work
NENU-500	0.36	GCE	237	96	18
NENU-501	0.36	GCE	392	137	18
NiP_2Mo_5	0.28	GCE	255	122	19
S-NiP_2Mo_5	0.28	GCE	85	46	19
HUST-200	0.35	GCE	131	51	20
Cu_2W_6	-	GCE	146	69	21
1-CP	0.13	Carbon paper	417	68	22
$NiMo_6O_{24}$@Cu/TNA	4 ± 0.2	GCE	215	89	23
$Mn_4V/CoSe_2$ NBs	1.02	GCE	187	55	24
1/CC	10	Carbon cloth	164.2	246.2	2
HUST-100	0.35	GCE	234	82	25
1-CP	0.23	Carbon paper	120	112	26
1-CC	-	Carbon cloth	480	151	27
P_8W_{48}/rGO	0.3	RDE	28	38	28
P_2W_{18}@rGF_ox	0.5	GCE	35	37	29
P_5W_{30}@rGF_ox	0.5	GCE	33	33	29
P_8W_{48}@rGF_ox	0.5	GCE	44	41	29

Notes: overpotential η_{10} at the current density of 10 mA cm^{-2}.

Table S8 Comparison of HER performance of **1-**AC-RDE and **2-**AC-RDE with other Ag-based HER electrocatalysts in acidic electrolyte

Catalyst	Loading (mg cm^{-2})	Electrode	η_{10} (mV)	Tafel slope (mV dec^{-1})	Reference
1-AC-RDE	0.32	RDE	112	77	This work
2-AC-RDE	0.32	RDE	91	65	This work
MoO_3 /Ag	–	GCE	145	43	30
$AgBr_{800}$	–	GCE	108	119	31
Pristine Ag	–	GCE	–	98	17
1T-MoS_2@Ag/Au NPs	–	GCE	201	53	32
$Pd_{68}Ag_{32}$	0.71	GCE	176	101.4	32
$Pd_{43}Ag_{21}Pt_{36}$	0.71	GCE	9	19.6	33
8 wt% Ag/MoS_2	~2.1	RDE	230	109	34
Ag foil	0.2	GCE	614	231	35
Ag-200	0.2	GCE	233	82	35
L-Ag NPs	0.2	GCE	32	31	35
20Ag@CN	9	ITO	213	250	36
Hb/20Ag@CN	9	ITO	79	155	36
P-Ag@NC	0.8	GCE	78	107	37
Nanoporous Ag foam	0.245	Carbon fiber	362	136	38

Notes: overpotential η_{10} at the current density of 10 mA cm^{-2}.

Table S9 Summary of HER performances of different electrocatalysts in 0.5 M H_2SO_4

Catalyst	η_{10} (mV)	η_{50} (mV)	Tafel slope (mV dec^{-1})	j_0 (mA cm^{-2})	R_{ct} (Ω)
1-AC-RDE	112	206	77	0.3414	5.72
2-AC-RDE	91	192	65	0.4480	5.11
Ag-H_2biim-RDE	334	456	127	0.0668	74.52
SiW_{12}-H_2biim-RDE	530	677	147	0.0117	50.26
P_2W_{18}-H_2biim-RDE	490	635	136	0.0359	19.18
Pt/C	51	121	37	–	–

Notes: overpotential η_{10} and η_{50} at the current density of 10 and 50 mA cm^{-2}, respectively.

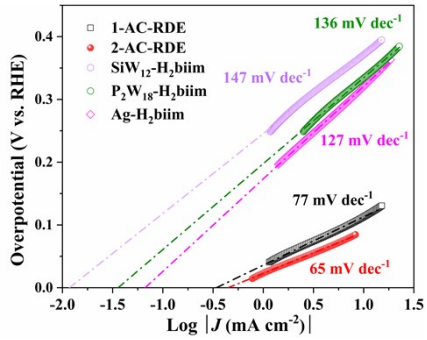

Fig. S15 Exchange current density (j_0) of different catalysts modified RDE in 0.5 M H_2SO_4.

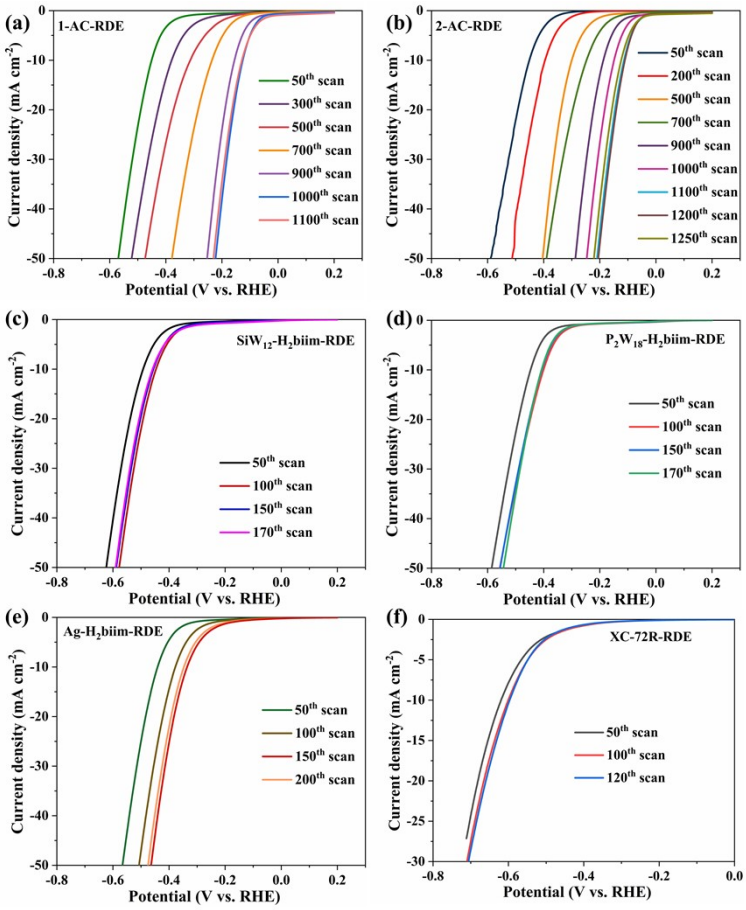

Fig. S16 LSV curves of (a) **1-**AC-RDE, (b) **2-**AC-RDE, (c) SiW_{12}-H_2biim-RDE, (d) P_2W_{18}-H_2biim-RDE, (e) Ag-H_2biim-RDE and (f) XC-72R-RDE after different times of successive CV cycles using graphite rod instead of Pt wire as the counter electrode in 0.5 M H_2SO_4, scan rate: 5 mV s^{-1}.

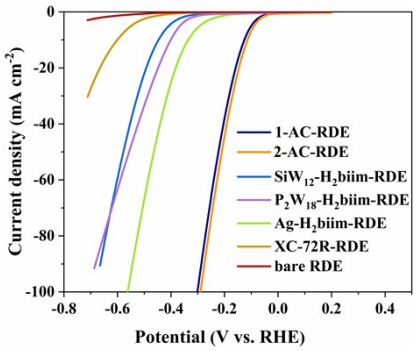

Fig. S17 LSV curves of different catalysts modified RDE using graphite rod as counter electrode in 0.5 M H_2SO_4

Table S10 Summary of HER performances of different electrocatalysts using graphite rod as counter electrode in 0.5 M H_2SO_4

Catalyst	η_{10} (mV)	η_{50} (mV)
1-AC-RDE	125	223
2-AC-RDE	114	210
Ag-H_2biim-RDE	336	464
SiW_{12}-H_2biim-RDE	446	578
P_2W_{18}-H_2biim-RDE	401	557
XC-72R	599	-
Bare RDE	-	-

Notes: overpotential η_{10} and η_{50} at the current density of 10 and 50 mA cm^{-2}, respectively

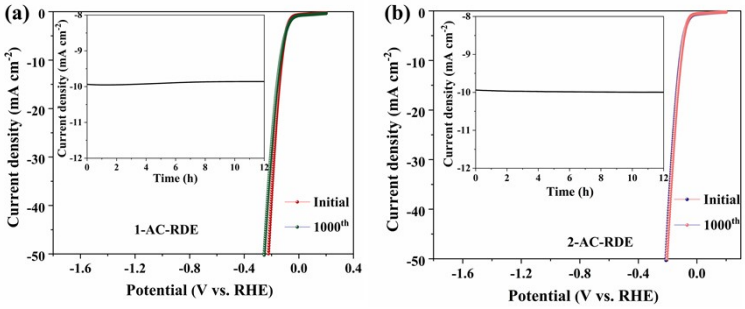

Fig. S18 LSV curves of (a) **1**-AC-RDE and (b) **2**-AC-RDE before and after 1000 times of CV sweeps (inset: chronoamperometric curves) using graphite rod as counter electrode.

7. Characterizations toward HER analysis

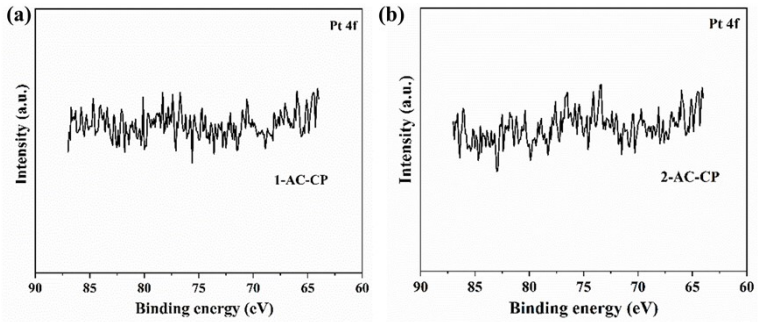

Fig. S19 XPS spectra of **1**-AC-CP and **2**-AC-CP for Pt 4f.

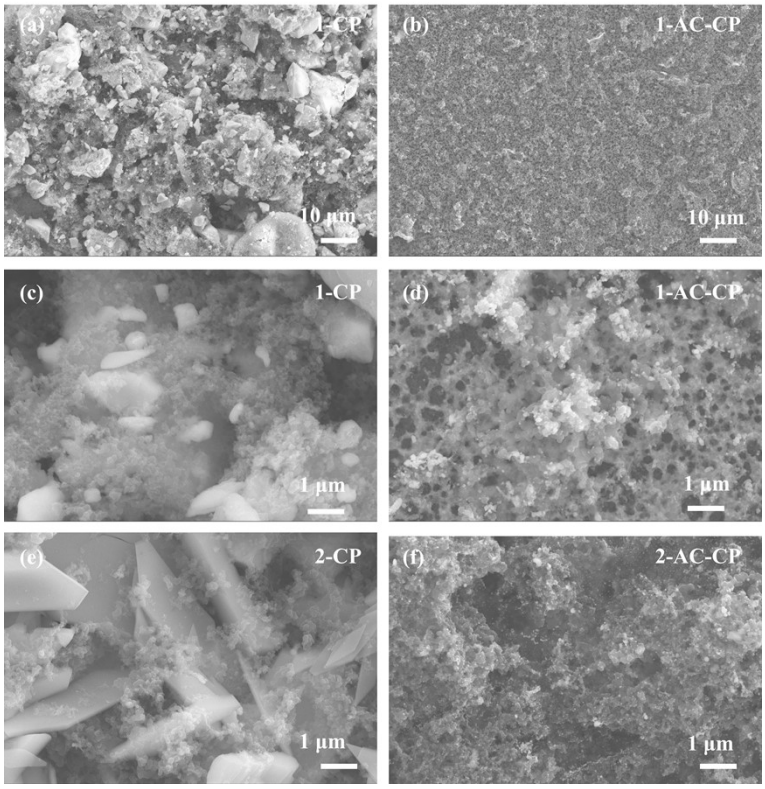

Fig. S20 SEM image of (a, c) **1**-CP, (b, d) **1**-AC-CP, (e) **2**-CP and (f) **2**-AC-CP.

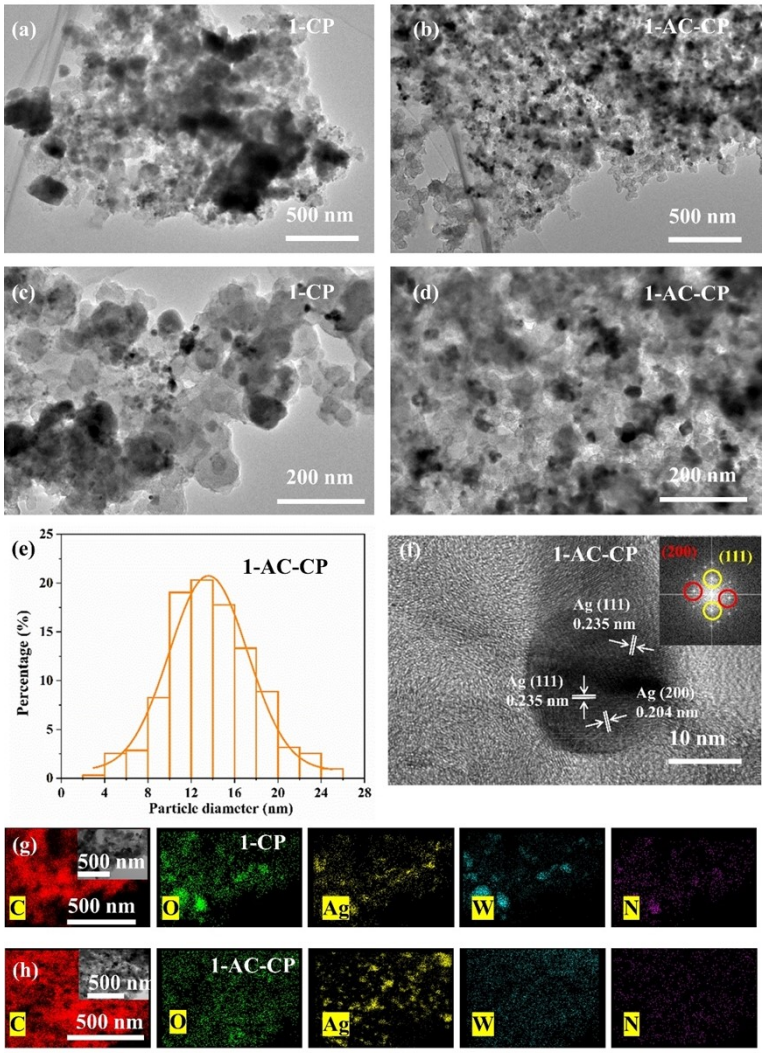

Fig. S21 TEM images of (a, c) **1**-CP and (b, d) **1**-AC-CP, e) particle size distribution of **1**-AC-CP, (f) HR-TEM image of **1**-AC-CP (inset is FFT image), elemental mappings of (g, h) C, O, Ag, W and N in **1**-CP and **1**-AC-CP, respectively.

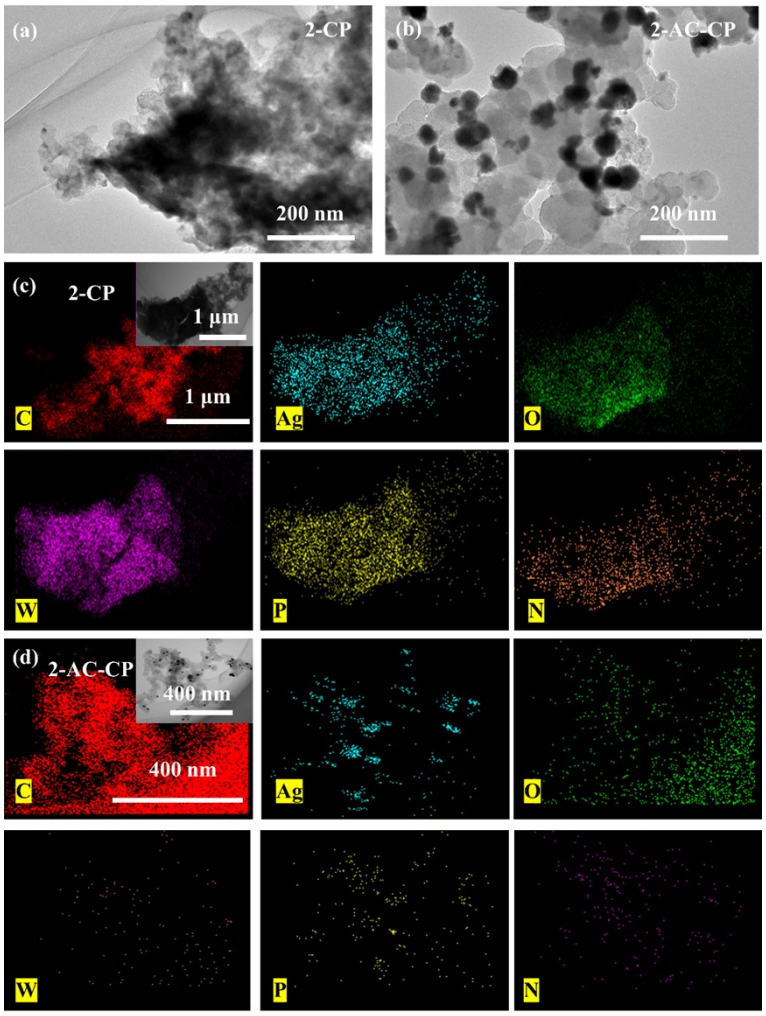

Fig. S22 TEM images of (a) **2**-CP and (b) **2**-AC-CP, elemental mappings of (c, d) C, O, Ag, W and N in **2**-CP and **2**-AC-CP, respectively.

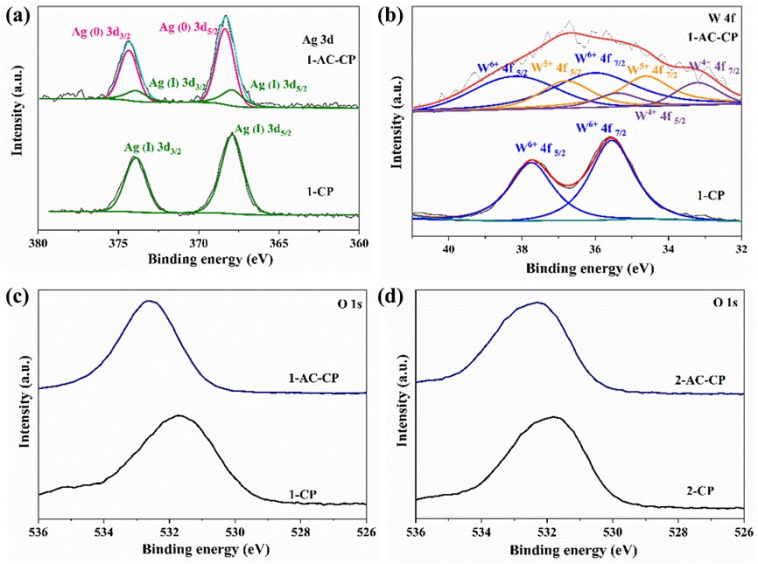

Fig. S23 XPS spectra of **1**-CP, **2**-CP, **1**-AC-CP and **2**-AC-CP for (a) Ag 3d, (b) W 4f and (c-d) O 1s.

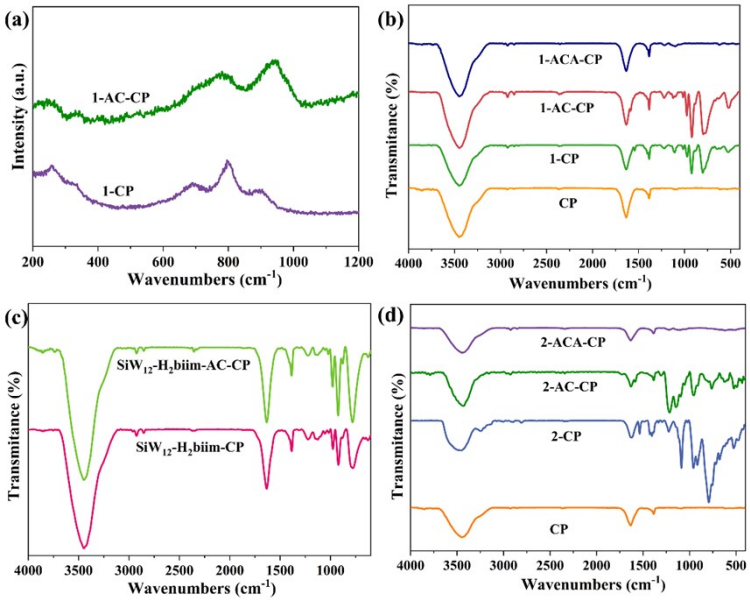

Fig. S24 (a) Raman spectra of **1**-CP and **1**-AC-CP and (b) FTIR spectrum of the carbon paper, **1**-CP, **1**-AC-CP and **1**-ACA-CP that represents **1**-AC-CP was treated in 0.1 M KOH for 4h and (c) FTIR spectrum of the fresh and activated SiW_{12}-H_2biim-CP and (d) the carbon paper, **2**-CP, **2**-AC-CP and **2**-ACA-CP that represents **2**-AC-CP was treated in 0.1 M KOH for 4h.

Table S11 Calculation of Ag and W percentage leached into electrolyte from **1**-CP and **2**-CP after the electrochemical restructuring based on ICP-OES data

Electrode	Mass on the electrode before electrochemical restructuring (mg)		Mass in the electrolyte after electrochemical restructuring (mg)		Leaching percentage (%)	
	Ag	**W**	**Ag**	**W**	**Ag**	**W**
1-CP	0.04312	0.22040	0.00031	0.06064	0.72	27.50
2-CP	0.03168	0.24312	0.00033	0.06490	1.04	26.69

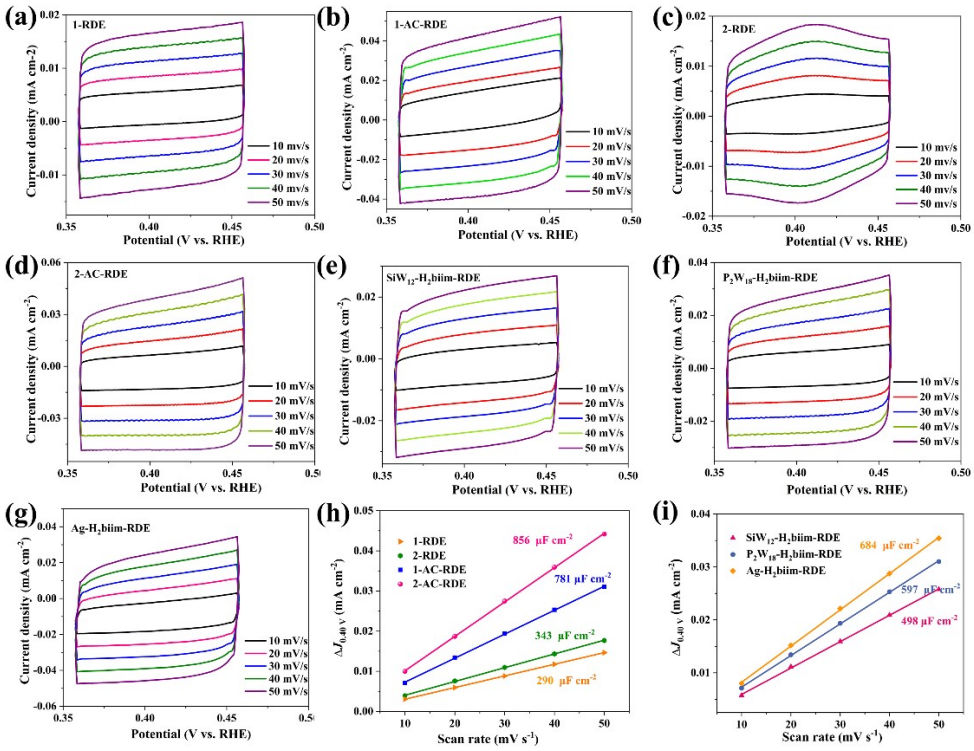

Fig. S25 (a-g) CV curves at non-faradaic potentials of different catalysts modified RDE with scan rates from 10 to 50 mV s^{-1} and (h, i) the capacitive current at 0.4 V (vs. RHE) as a function of scan rate for different catalysts modified RDE.

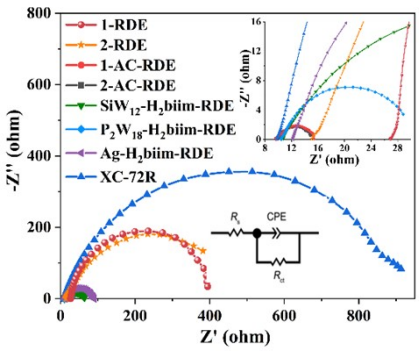

Fig. S26 Nyquist plots of different catalysts modified RDE in 0.5 M H_2SO_4, (inset is the magnified images of low frequency region and the equivalent circuit used to fit Nyquist plots) .

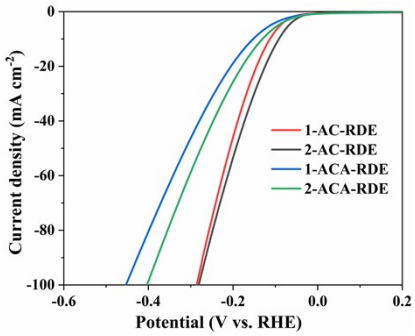

Fig. S27 LSV curves of **1-**AC-RDE, **2-**AC-RDE, **1-**ACA-RDE and **2-**ACA-RDE.

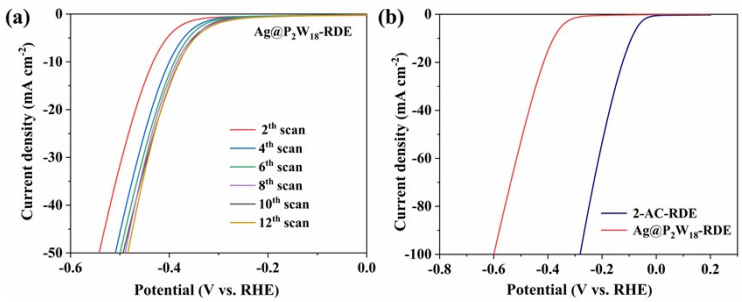

Fig. S28 LSV curves of (a) Ag@P_2W_{18}-RDE and (b) different catalysts modified RDE in 0.5 M H_2SO_4, scan rate: 5 mV s^{-1}.

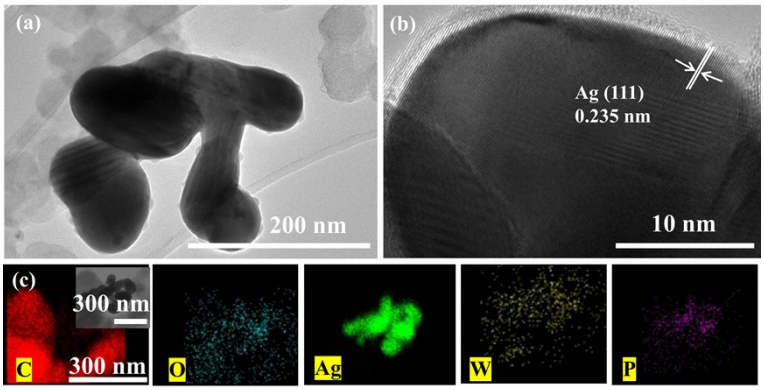

Fig. S29 HR-TEM images of (a, b) Ag@P_2W_{18}-CP and elemental mappings of (c) C, O, Ag, W and P in Ag@P_2W_{18}-CP, respectively.

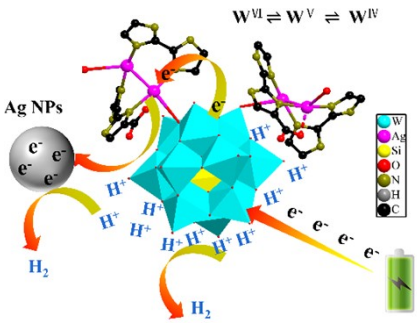

Fig. S30 Possible electrochemical surface restructuring process for compound **1**.

8. References

1 H. H. Thorp, *Inorg. Chem*., 2002, **31**, 1585−1588.
2 X. L. Wang, Y. Tian, Z. H. Chang and H. Lin, *ACS Sustain. Chem. Eng*., 2020, **8**, 15696-15702.
3 B. Dong, J. Peng, P. Zhang, A. Tian, J. Chen and B. Xue, *Inorg. Chem. Commun*., 2007, **10**, 839-842.
4 Y. Gong, Y. X. Yang, M. M. Zhang, X. L. Gao, J. L. Yin and J. H. Lin, *Dalton Trans*., 2014, **43**, 16928-16936.
5 Y. Liang, S. Di, C. Wang, K. Yu, C. Wang, J. Lv and B. Zhou, *J. Energy Storage*, 2022, **56**, 105991.
6 Zhang, G. Wang, D. Chen, X. Lv and J. Li, *Chem. Mater*., 2008, **20**, 6543—6549.
7 H. Yan, C. Tian, L. Wang, A. Wu, M. Meng, L. Zhao and Fu, H. Angew Chem. Int. Ed., 2015, 54, 6325—6329.
8 J. Du, Z. L. Lang, Y. Y. Ma, H. Q. Tan, B. L. Liu, Y. H. Wang, Z. H. Kang and Y. G. Li, *Chem. Sci*., 2020, **11**, 3007—3015.
9 L. Li, C. Tang, Y. Zheng, B. Xia, X. Zhou, H. Xu and Qiao, S. Z. *Adv. Energy Mater*., 2020, **10**, 2000789.
10 Y. Sun, L. Silvioli, N. R. Sahraie, W. Ju, J. Li, A. Zitolo, S. Li, A. Bagger, L. Arnarson, X. Wang, T. Moeller, D. Bernsmeier, J. Rossmeisl, F. Jaouen and P. Strasser, *J. Am. Chem. Soc*., 2019, **141**, 12372—12381.
11 S. Cai, S. Shi, H. Li, Y. Bai and D. Dang, *Res. Chem. Intermed*., 2018, **44**, 7769—7788.
12 A. Bar-Hen, S. Hettler, A. Ramasubramaniam, R. Arenal, R. Bar-Ziv and M. Bar. Sadan, *J. Energy Chem*., 2022, **74**, 481—488.
13 M. Sadakane and E. Steckhan, *Chem. Rev*., 1998, **98**, 219−238.
14 P. D. Prenzler, C. Boskovic, A. M. Bond and A. G. Wedd, *Anal. Chem*., 1999, **71**, 3650−3656.
15 J. Sha, J. Peng, Y. Lan, Z. Su, H. Pang, A. Tian, P. Zhang and M. Zhu, *Inorg. Chem*., 2008, **47**, 5145−5153.
16 X. Liu, L. Cui, K. Yu, J. Lv, Y. Liu, Y. Ma and B. Zhou, *Inorg. Chem*., 2021, **60**, 14072−14082.
17 L. Cheng, X. Zhang, X. Xi, B. Liu and S. Dong, *J. Electroanal. Chem*., 1996, **407**, 97−103.
18 J. S. Qin, D. Y. Du, W. Guan, X. J. Bo, Y. F. Li, L. P. Guo, Z. M. Su, Y. Y. Wang, Y. Q. Lan and H. C. Zhou, *J. Am. Chem. Soc*., 2015. **137**, 7169-7177.
19 Y. Zheng and X. Xu, *ACS. Appl. Mater. Interfaces*, 2020, **12**, 53739−53748.
20 L. Zhang, S. Li, C. J. Gomez-Garcia, H. Ma, C. Zhang, H. Pang and B. Li, *ACS Appl Mater. Interfaces*, 2018, **10**, 31498-31504.
21 Q. Shen, C. Zhang, M. Wang, H. Pang, H. Ma, X. Wang, L. Tan, D. Chai, Y. Hou and B. Li, Inorg. Chem. Commun., 2019, 99, 64-69.
22 Y. X. Ding, Q. H. Zheng, M. T. Peng, C. Chen, K. F. Zou, B. X. Dong, W. L. Liu and Y. L. Teng, *Catal. Commun*., 2021, **161**, 106367.
23 D. Zang, Y. Huang, Q. Li, Y. Tang and Y. Wei, *Appl. Catal. B: Environ*., 2019, **249**, 163−171.
24 W. Ahmad, Q. Gao, X. L. Zhang, W. Tan, L. Zhang, M. R. Gao and S. H. Yu, *ChemNanoMat*., 2020, **6**, 1164-1168.
25 S. Li, L. Zhang and Y. Lan, *Chem. Commun*., 2018, **54**, 1964−1967.
26 P. Wang, H. Zhang, P. Wang, J. Zha, J. Gautam, H. Zhang, R. Li, L. N. Zhang, G. Diao and L. Ni, Catal. Commun., 2022, **165**, 106446.
27 Y. C. Zhang, Y. Tian, Z. H. Chang, Q. Q. Liu, Y. Z. Chen, J. N. Wang and X. L. Wang, *Eur. J. Inorg. Chem*., 2022, 2, e202100725.
28 R. Liu, G. Zhang, H. Cao, S. Zhang, Y. Xie, A. Haider, U. Kortz, B. Chen, N. S. Dalal, Y. Zhao, L. Zhi, C.-X. Wu, L.-K. Yan, Z. Su and B. Keita, *Energy Environ. Sci*., 2016, **9**, 1012−1023.
29 D. M. Fernandes, M. P. Araújo, A. Haider, A. S. Mougharbel, A. J. S. Fernandes, U. Kortz and C. Freire, *ChemElectroChem*, 2018, **5**, 273−283.
30 X. Xia, X. Shen, X. Zhao, W. Ye and C. Wang, ChemCatChem, 2015, 7, 2517−2525.
31 J. F. Huang and Y. C. Wu, *ACS Sustain. Chem. Eng*., 2018, **6**, 8285−8290.
32 J. Wang, W. Fang, Y. Hu, Y. Zhang, J. Dang, Y. Wu, H. Zhao and Z. Li, *Catal. Sci. Technol*., 2020, **10**, 154-163.
33 W. Lu, X. Xia, X. Wei, M. Li, M. Zeng, J. Guo and S. Cheng, *ACS Appl. Mater. Interfaces*, 2020, **12**, 21569−21578.
34 M. Ghosal Chowdhury, L. Sahoo, S. Maity, D. Bain, U. K. Gautam and A. Patra, *ACS Appl. Nano Mater*., 2022, **5**, 7132−7141.
35 Z. Li, J. Y. Fu, Y. Feng, C. K. Dong, H. Liu and X. W. Du, Nat. Catal., 2019, 2, 1107−1114.
36 D. Rodriguez-Padron, A. R. Puente-Santiago, M. Cano, A. Caballero, M. J. Munoz-Batista and R. Luque, *ACS Appl. Mater. Interfaces*, 2020, **12**, 2207−2215.
37 X. Ji, B. Liu, X. Ren, X. Shi, A. M. Asiri and X. Sun, *ACS Sustain. Chem. Eng*., 2018, **6**, 4499−4503.
38 J. Lu, J. Guo, S. Song, G. Yu, H. Liu, X. Yang and Z. Lu, *RSC Adv*., 2020, **10**, 38583−38587.